Active Contour External Force Using Vector Field Convolution for Image Segmentation

Bing Li, *Student Member, IEEE*, and Scott T. Acton, *Senior Member, IEEE*

***Abstract*—Snakes, or active contours, have been widely used in image processing applications. Typical roadblocks to consistent performance include limited capture range, noise sensitivity, and poor convergence to concavities. This paper proposes a new external force for active contours, called vector field convolution (VFC), to address these problems. VFC is calculated by convolving the edge map generated from the image with the user-defined vector field kernel. We propose two structures for the magnitude function of the vector field kernel, and we provide an analytical method to estimate the parameter of the magnitude function. Mixed VFC is introduced to alleviate the possible leakage problem caused by choosing inappropriate parameters. We also demonstrate that the standard external force and the gradient vector flow (GVF) external force are special cases of VFC in certain scenarios. Examples and comparisons with GVF are presented in this paper to show the advantages of this innovation, including superior noise robustness, reduced computational cost, and the flexibility of tailoring the force field.**

***Index Terms*—Active contours, deformable models, external force, gradient vector flow (GVF), snakes, vector field convolution (VFC).**

I. Introduction

ACTIVE *models* [1], or *deformable models* [2], have been widely used for image segmentation [3]–[6] and objects tracking [7]–[10]. Although there are several existing modified version of active models [11]–[14], the most widely used active models include *active contours* (also known as *snakes* or *deformable contours*) [1] and *active surfaces* (also known as *deformable surfaces*) [2]. The active models deform on the image domain and capture a desired feature by minimizing an energy functional subject to certain constraints. The energy functional usually contains two terms: an internal energy, which constrains the smoothness and tautness of the model, and an external energy, which attracts the elastic model to the *features of interest* (FOI). We focus on parametric active contours [1] and discrete active surfaces [4], [15] in this paper, though the result could be generalized to other active models.

Manuscript received Septembr 12, 2006; revised April 19, 2007. This work was supported in part by the National Institutes of Health (EB001826) and in part by the U.S. Army Research Office (46850-CI). The associate editor coordinating the review of this manuscript and approving it for publication was Dr. Gaudenz Danuser.

B. Li is with the C. L. Brown Department of Electrical and Computer Engineering, University of Virginia, Charlottesville, VA 22904 USA (e-mail: bingli@virginia.edu).

S. T. Acton is with the C. L. Brown Department of Electrical and Computer Engineering/Biomedical Engineering, University of Virginia, Charlottesville, VA 22904 USA (e-mail: acton@virginia.edu).

Color versions of one or more of the figures in this paper are available online at http://ieeexplore.ieee.org.

Digital Object Identifier 10.1109/TIP.2007.899601

An external force for snakes, called *gradient vector flow* (GVF) [16] and its improved version [17], were introduced to overcome two key difficulties of snakes. The snake using the GVF field provides a large capture range and the ability to capture concavities by diffusing the gradient vectors of an edge map generated from the image. Although the GVF field has been widely used and improved in various models [7], [9], [18], there are some disadvantages, such as high computational cost, noise sensitivity, parameter sensitivity, and the ambiguous relationship between the capture range and parameters.

In this paper, we present a novel external force for active models called *vector field convolution* (VFC) to address the above problems. This external force is calculated by convolving a vector field with the edge map derived from the image. Active contours that use VFC external force are termed VFC snakes. Like GVF snakes, instead of being formulated using the standard energy minimization framework, VFC snakes are constructed by way of a force balance condition.

The VFC snakes have not only a large capture range and ability to capture concavities, but also better robustness to noise and initialization, flexibility of tailoring the force field, and reduced computational cost [19]. Those advantages are demonstrated by examples and comparisons with GVF snakes in Section IV.

II. Background

A. Parametric Active Contours

An active contour is represented by a parametric curve $\mathbf{v}(s) = [x(s), y(s)]^T, s \in [0, 1]$ that deforms through the image domain to minimize the energy functional [1]

$$E_{\text{ac}} = \int_0^1 \left[\frac{1}{2}(\alpha|\mathbf{v}'(s)|^2 + \beta|\mathbf{v}''(s)|^2) + E_{\text{ext}}(\mathbf{v}(s)) \right] ds \tag{1}$$

where α and β are weighting parameters representing the degree of the smoothness and tautness of the contour, respectively, and $\mathbf{v}'(s)$ and $\mathbf{v}''(s)$ are the first and second derivatives of $\mathbf{v}(s)$ with respect to s. E_{ext} denotes the external energy, the value of which is small at the FOI, such as edges [16]. Typical external energies for a gray-level image $I(x, y)$ for seeking the edges are given as [1]

$$E_{\text{ext}}^{(1)}(x, y) = -|\nabla I(x, y)|^2 \tag{2}$$

$$E_{\text{ext}}^{(2)}(x, y) = -|\nabla [G_\sigma(x, y) * I(x, y)]|^2 \tag{3}$$

where $G_\sigma(x, y)$ is a 2-D Gaussian function with standard deviation σ, $*$ denotes linear convolution, and ∇ denotes the gradient operator. If the image is a binary image, where the FOI are ones

and the background is zero-valued, the typical external energies are given as [20]

$$E_{\text{ext}}^{(3)}(x,y) = -I(x,y), \tag{4}$$

or

$$E_{\text{ext}}^{(4)}(x,y) = -G_\sigma(x,y) * I(x,y). \tag{5}$$

Although a large σ may distort the FOI, a large σ is often necessary to suppress the noise and increase the capture range of the active contours.

At the minima of (1), the contour must satisfy the Euler–Lagrange equation

$$\alpha\mathbf{v}'' - \beta\mathbf{v}'''' - \nabla E_{\text{ext}}(\mathbf{v}) = 0 \tag{6}$$

which can be considered as a force balance equation

$$\mathbf{f}_{\text{int}}(\mathbf{v}) + \mathbf{f}_{\text{ext}}(\mathbf{v}) = 0 \tag{7}$$

where $\mathbf{f}_{\text{int}}(\mathbf{v}) = \alpha\mathbf{v}'' - \beta\mathbf{v}''''$ is the internal force to constraint the contour smoothness and tautness, and $\mathbf{f}_{\text{ext}}(\mathbf{v}) = -\nabla E_{\text{ext}}(\mathbf{v})$ is the external force that attracts the contour toward the FOI. To solve (6), $\mathbf{v}(s)$ is treated as a function of time t. The solution is obtained when the steady state solution of the following gradient descent equation:

$$\frac{\partial \mathbf{v}(s,t)}{\partial t} = \alpha\mathbf{v}''(s,t) - \beta\mathbf{v}''''(s,t) + \mathbf{f}_{\text{ext}}(\mathbf{v}(s,t)) \tag{8}$$

is reached from an initial contour $\mathbf{v}(s,0)$.

A numerical solution to (8) on a discrete grid can be achieved by solving a discretization of s iteratively using a finite difference approach [1], [20]. The continuous contour $\mathbf{v}(s), s \in [0,1]$ is sampled and represented by a set of m discrete points $\mathbf{v}_i, i \in \{0,1,\ldots,M-1\}$. These sample points are referred to as *snake elements*, or *snaxels*. The update procedure for the entire contour can be written in matrix form as

$$(\mathbf{I} + \tau\mathbf{A})\mathbf{V}^{t+1} = \mathbf{V}^t + \tau\mathbf{F}^t \tag{9}$$

where $\mathbf{I}$ is the $M \times M$ identity matrix, $\mathbf{V}^t = [\mathbf{v}_0^t, \mathbf{v}_1^t, \ldots, \mathbf{v}_{M-1}^t]^T$ and $\mathbf{F}^t = [\mathbf{f}_{\text{ext}}(\mathbf{v}_0^t), \mathbf{f}_{\text{ext}}(\mathbf{v}_1^t), \ldots, \mathbf{f}_{\text{ext}}(\mathbf{v}_{M-1}^t)]^T$ are $M \times 2$ matrices representing the positions and the external forces of snaxels at time t, respectively. $\mathbf{A}$ is an $M \times M$ cyclic pentadiagonal matrix used to compute the internal force. Note that, since $(\mathbf{I} + \tau\mathbf{A})$ is a cyclic symmetric pentadiagonal positive definite matrix, we could use either Cholesky decomposition [21] or the algorithm proposed in [22] to solve $\mathbf{V}^{t+1}$ efficiently.

B. External Forces

A number of research groups have generalized (7) via replacing the standard external force by the sum of other forces generated from the image and/or the contour [16], [20], [23]. Instead of a standard energy minimization problem, the solution of the snake is formulated as a force balance equation. Different external forces have been proposed to improve the performance of snakes. The external forces can be generally classified as dynamic forces and static forces [16]. The dynamic forces are those that depend on the snake and, as a result, change as the snake deforms. The static forces are those that are calculated from the image, and remain unchanged as the snake deforms. The static forces can be further classified based on the force sources. Edge-based static forces are calculated from the image edges, whereas region-based static forces are computed using the region intensity and/or texture information [24].

The *pressure force*, also known as the *inflation force*, used in balloon models is an useful dynamic force that pushes the snake either outward (inflation) or inward (deflation) [6], [15], [20], [23], [25]. Although the pressure force can avoid spurious edges, the pressure force causes leakage problem when there are significant gaps in the edges [16]. Another limitation of the snake using a pressure force is that it must be initialized either inside or outside the targeted object.

A desirable static force should have an important property: a free particle placed in the force field should be able to move to the FOI, such as edges. A free particle is defined as a single point snake with no internal force. The major drawback of standard external forces is that the force field has an initially zero magnitude in the homogeneous regions of the image. Therefore, the initial snake must be close to the FOI in order to converge. One way to alleviate this problem is to increase the standard deviation of the Gaussian filter used in the external energy, with the cost of distorting the FOI. Several methods have been proposed to guide the particles in homogeneous regions to the FOI. The *distance forces* are proposed to solve this problem by making the force point to the closest "edge point," which significantly increases the capture range of the FOI [20]. The edge points are extracted from edge detector, such as the Canny edge detector [26]. The distance forces are calculated by taking the negative derivative of the distance transformation of the edge points [20].

The *gradient vector flow* (GVF) field is another edge-based static force defined by the vector field $\mathbf{f}_{\text{gvf}}(x,y) = [u_{\text{gvf}}(x,y), v_{\text{gvf}}(x,y)]$ that minimizes the energy functional

$$E_{\text{gvf}} = \iint [\mu(|\nabla u_{\text{gvf}}|^2 + |\nabla v_{\text{gvf}}|^2) + |\nabla f|^2 |\mathbf{f}_{\text{gvf}} - \nabla f|^2] dx dy \tag{10}$$

where f is an *edge map* derived from the image, and μ is a parameter controlling the degree of smoothness of the GVF field. The edge map f is typically the additive inverse of an external energy such as that given in (2)–(5). The GVF field outperforms the distance forces by providing a large capture range and the ability to capture boundary concavities [16]. The generalized GVF (GGVF) field, a generalization of the GVF formulation, improves the ability to capture narrow boundary concavities [17]. Although the GVF field has these desired properties, there are still several unsolved problems, such as the ambiguous relationship between the capture range and the parameters, the sensitivity to the parameters and noise, especially impulse noise, and expensive computational cost.

The calculation of the external force can be broken down to two independent steps: the formation of edge map from the image, and the computation of the external force from the edge map. Although the quality of the edge map is a critical factor in

snake performance, this paper focuses on how to obtain a desirable external force field given an edge map, which is likely to be corrupted by noise. We propose a new class of edge-based static forces called *vector field convolution* (VFC) in this paper. This new external force is calculated by convolving a vector field kernel with the edge map [19]. The novel static external force has not only a large capture range and ability to capture concavities, but also reduced computational cost, superior robustness to noise and initialization, flexibility of changing the force field. We demonstrate these desirable properties by comparing VFC with GVF in Section IV. (Note that we can always combine VFC with a region-based static or dynamic force model.) The fundamental difference between the distance forces, the GVF forces and the VFC forces lies in the method with which the homogeneous regions are filled.

III. Vector Field Convolution Snakes

Vector field convolution snakes are active contours using the VFC field as the external force. By replacing the standard external force $\mathbf{f}_{\text{ext}}(\mathbf{v}) = -\nabla E_{\text{ext}}(\mathbf{v})$ in (8) by the VFC field $\mathbf{f}_{\text{vfc}}(\mathbf{v})$, the iterative snakes solution is

$$\frac{\partial \mathbf{v}(s,t)}{\partial t} = \alpha \mathbf{v}''(s,t) - \beta \mathbf{v}''''(s,t) + \mathbf{f}_{\text{vfc}}(\mathbf{v}(s,t)). \quad (11)$$

This equation can be solved numerically using identical finite difference approach of standard snakes given in Section II-A.

A. Vector Field Convolution

A new class of static external forces called *vector field convolution* (VFC) is introduced in this section. We first define a *vector field kernel* $\mathbf{k}(x,y) = [u_k(x,y), v_k(x,y)]$ in which all the vectors point to the kernel origin

$$\mathbf{k}(x,y) = m(x,y)\mathbf{n}(x,y) \quad (12)$$

where $m(x,y)$ is the magnitude of the vector at (x,y) and $\mathbf{n}(x,y)$ is the unit vector pointing to the kernel origin $(0,0)$

$$\mathbf{n}(x,y) = [-x/r, -y/r] \quad (13)$$

except that $\mathbf{n}(0,0) = [0,0]$ at the origin, where $r = \sqrt{x^2+y^2}$ is the distance from the origin. If the origin is considered as the FOI, this vector field kernel has the desirable property that a free particle placed in the field is able to move to the FOI, such as edges. Note that the kernel origin is not the origin of the image or the edge map.

The VFC external force $\mathbf{f}_{\text{vfc}}(x,y) = [u_{\text{vfc}}(x,y), v_{\text{vfc}}(x,y)]$ is given by calculating the convolution of the vector field kernel $\mathbf{k}(x,y)$ and the edge map $f(x,y)$ generated from the image $I(x,y)$

$$\begin{aligned}\mathbf{f}_{\text{vfc}}(x,y) &= f(x,y) * \mathbf{k}(x,y) \\ &= [f(x,y) * u_k(x,y), f(x,y) * v_k(x,y)].\end{aligned} \quad (14)$$

Since the edge map is non-negative and larger near the image edges, edges contribute more to the VFC than homogeneous regions. Therefore, the VFC external force will attract free particles to the edges. If we represent the vector field kernel using a complex-valued range, the VFC is just the filtering result of the edge map, which does not depend on the origin of the kernel.

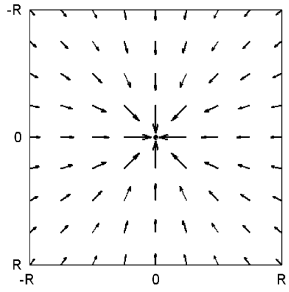

Fig. 1. Example discrete vector field kernel with $R = 4$.

The VFC field highly depends on the magnitude of the vector field kernel $m(x,y)$. By considering the fact that the influence from the FOI should decrease as the particles are further away, the magnitude should be a decreasing positive function of distance from the origin. We propose two types of magnitude functions, given as

$$m_1(x,y) = (r+\varepsilon)^{-\gamma} \quad (15)$$

$$m_2(x,y) = \exp(-r^2/\zeta^2) \quad (16)$$

where γ and ζ are positive parameters to control the decrease, ε is a small positive constant to prevent division by zero at the origin. $m_1(x,y)$ is inspired by Newton's law of universal gravitation in physics, which can be viewed as a special case with $\gamma = 2$ and $\varepsilon = 0$. Then, edge pixels in the edge map may be considered objects with mass proportional to the edge strength, and the VFC field is the gravity field generated by all objects. The influence of the FOI increases as γ decreases. In practice, γ usually ranges from 1.5 to 3 for most images. $m_2(x,y)$ is a Gaussian shape function, where ζ can be viewed as the standard deviation. The influence of the FOI increases as ζ increases. Note that the external force proposed in [27] is a special case of $m_1(x,y)$ with $\gamma = 2$. In general, the influence of the FOI should be increased (decrease γ or increase ζ) as the signal-to-noise ratio (SNR) is decreased.

B. Numerical Implementation

The continuous vector field kernel $\mathbf{k}(x,y)$ is approximated by a discrete and finite matrix given as

$$\mathbf{K} = \{\mathbf{k}(x,y); x,y = -R, \ldots, -1, 0, 1, \ldots, R\} \quad (17)$$

where R denotes the preferred kernel radius. An example discrete vector field kernel is demonstrated in Fig. 1. To calculate the VFC field, each component of the discrete vector field kernel is convolved with the edge map. The discrete linear convolution has been well studied and can be accelerated by the fast Fourier transform (FFT) and the inverse fast Fourier transform (IFFT) [28]. Furthermore, if we treat the vectors as complex numbers instead of two separated real numbers, we could save the computational expense roughly by a factor of two without using a specialized FFT for real numbers [29]. In our implementation, the external forces $\mathbf{f}_{\text{ext}}$ are normalized as unit vectors to encourage the contour evolves at a constant speed for an uniform time step

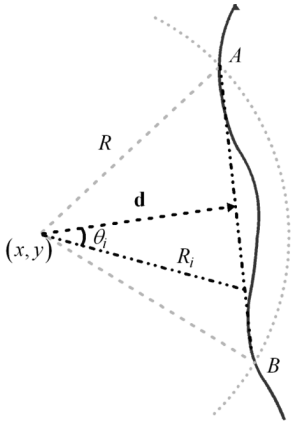

Fig. 2. Using a line $\overline{AB}$ to approximate the effective features of interest (FOI) $\widetilde{AB}$ of (x, y).

τ [20]. The MATLAB implementation of VFC and examples are available for download at http://viva.ee.virginia.edu/.

C. Parameter Estimation

To estimate the parameter γ of the vector field kernel for computing $m_1(x, y)$, we use a line $\overline{AB}$ to approximate the effective FOI $\widetilde{AB}$ of (x, y), as shown in Fig. 2. The effective FOI of (x, y) is defined as the FOI within R distance from (x, y). In order to capture free particles placed at (x, y), the VFC field should satisfy

$$\mathbf{f}_{\text{vfc}}(x,y)\cdot\mathbf{d}(x,y)>0 \quad \text{for } \|\mathbf{d}(x,y)\|=d\le R \tag{18}$$

where $\mathbf{d}(x, y)$ is the vector pointing to the approximated effective FOI $\overline{AB}$ of (x, y), the magnitude of which is the distance from the FOI. The VFC force can be decomposed into the force $\mathbf{f}_{\text{FOI}}(x, y)$ resultant from the FOI and the force $\mathbf{f}_{\text{noise}}(x, y)$ from the noise. The projection of these two forces in the $\mathbf{d}(x, y)$ direction leads to the scalar magnitudes $f_{\text{FOI}}(x, y)$ and $f_{\text{noise}}(x, y)$, respectively. The FOI force projection can be written as

$$\begin{aligned} f_{\text{FOI}}(x,y) &= \sum_{i:R_i\le R} f_i R_i^{-\gamma}\cos\theta_i \\ &= \sum_{i:R_i\le R} f_i R_i^{-\gamma}\frac{d}{R_i} \ge R^{-\gamma-1}d\sum_{i:R_i\le R} f_i \end{aligned} \tag{19}$$

where f_i is the magnitude of the i th FOI, R_i is distance from (x, y) to the i th FOI, θ_i is the angle between $\mathbf{d}(x, y)$ and the vector from (x, y) to the i th FOI. Equation (18) is satisfied if

$$R^{-\gamma-1}d\sum_{i:R_i\le R} f_i + f_{\text{noise}}(x,y) > 0. \tag{20}$$

If $f_{\text{noise}}(x, y) \ge 0$, (20) is fulfilled because $\sum_{i:R_i\le R} f_i > 0$. In the case that $f_{\text{noise}}(x, y) < 0, \gamma$ can be estimated using

$$\gamma < -1 + \log_R[-d\sum_{i:R_i\le R} f_i/f_{\text{noise}}(x,y)]. \tag{21}$$

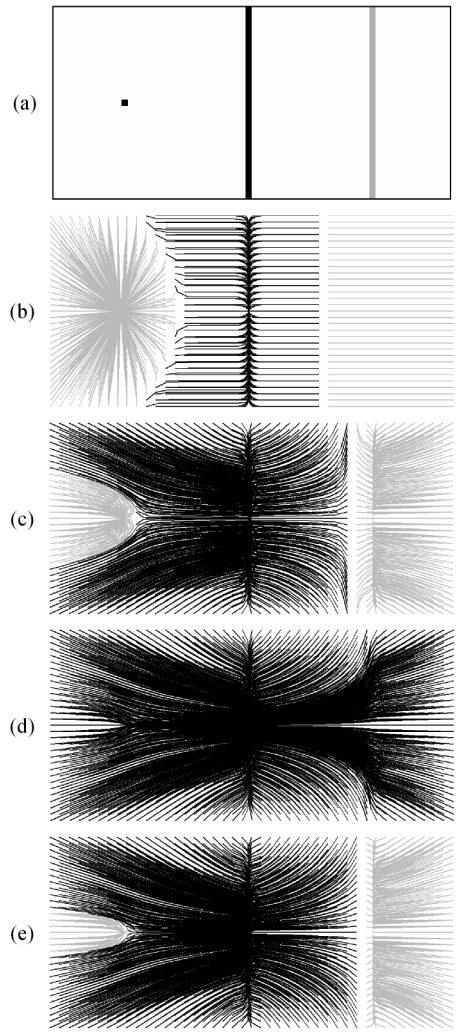

Fig. 3. (a) Synthetic edge map includes an impulse, a strong linear edge, and a weak linear edge from left to right, respectively. Streamlines generated from (b) the GVF field, the VFC fields using $m_1(x, y)$ with (c) $\gamma = 1.7$ and (d)$\gamma = 1.1$, and (e) the mixed VFC field that mixes (d) with the standard external forces. The streamlines converging to the strong edge are colored dark.

Hence, (21) provides an upper bound on γ for a desired capture range d. $\sum_{i:R_i\le R} f_i$ can be estimated by the product of the average magnitude and the length of AB, whereas f_{noise} can be estimated by the SNR of the image. This upper bound can be applied for meaningful selection of γ in an application where the desired capture range is known.

D. Mixed Vector Field Convolution

In the edge map generated from most images, the features can be roughly categorized as strong edges, weak edges, and noise. One major drawback of the GVF field is that it is very sensitive to noise, especially impulse noise because the vector diffusion process treats the gradients generated from different features equally. To demonstrate this problem, Fig. 3(a) shows a synthetic edge map, which includes an impulse noise, a strong edge, and a weak edge from left to right, respectively. The magnitude of the strong edge is equivalent to the magnitude of the noise, and four times as much as the magnitude of the weak edge. *Streamlines*, traces that exhibit where free particles move

when placed in a force field, are used for illustrating the force field [16]. The GVF field calculated from this edge map is illustrated in Fig. 3(b), where we can see that the strong edge and the impulse noise share the area between them equally. A similar scenario happens for the strong and weak edges. This phenomenon is usually undesirable in practice because snakes are designed to capture strong boundaries, which may or may not be the FOI.

The VFC field overcomes this problem because strong edges contribute more to the VFC field than weak edges and noise. As shown in Fig. 3(c), the capture range of the strong edge is significantly increased in the VFC field using magnitude function $m_1(x,y)$ with $\gamma = 1.7$. The majority of areas between the noise and the weak edge, and even half of the area on the left of the noise belongs to the capture range of the strong edge. Although the influence of the strong edge decreases as the particles are further away, the accumulated force of the strong edge is still able to overwhelm the force generated from the noise and the weak edge even if the particles are close to them. On a discrete grid, a possible extreme case is shown in Fig. 3(d). As the influence of the strong edge increases (because γ is reduced to 1.1 in this example), the right capture range of the noise is less than one pixel. As a result, the strong edge appears to dominate the whole image in the resulting discrete VFC field. Although the elimination of noise is desirable, weak edges are sometimes preferred to be preserved in practical applications, otherwise this might cause the leakage problem. To solve this dilemma, we propose to mix the VFC field with the standard external force, i.e., the gradient of the edge map f. The mixed VFC field $\mathbf{f}_{\text{mix}}(x,y)$ is defined as

$$\mathbf{f}_{\text{mix}}(x,y) = \begin{cases} \nabla f(x,y) & \|\nabla f(x,y)\| \geq \phi \\ \mathbf{f}_{\text{vfc}}(x,y) & \|\nabla f(x,y)\| < \phi \end{cases} \tag{22}$$

where ϕ is a threshold that determines the edges to preserve, which is similar to the smoothing parameter μ in GVF. Threshold selection methods for gray-level images, such as the Otsu method [30], can be employed to determine the threshold ϕ by treating $\|\nabla f(x,y)\|$ as a gray-level image. The mixed VFC field of Fig. 3(a) is shown in Fig. 3(e), where the weak edge is preserved and the noise has a diminished impact on the VFC field, which might be prevailed over by the internal force. The mixed VFC field can be viewed as the standard external force with homogeneous regions filled in by the VFC field.

E. Connections Between VFC and GVF

Note that there are two energy terms in the GVF energy functional of (10), the first of which diffuses the initial vector field, and the second term guarantees that the GVF field maintains the initial vector flow field components given before diffusion. In homogeneous regions of the image, the second term can be ignored because the gradient of the edge map is zero [16]. The numerical solution involves computing $\mathbf{f}_{\text{gvf}}(x,y)$ as function of time as follows:

$$\frac{\mathbf{f}_{\text{gvf}}(x,y,t+\Delta t) - \mathbf{f}_{\text{gvf}}(x,y,t)}{\Delta t} = \mu[\nabla^2 u_{\text{gvf}}(x,y,t), \nabla^2 v_{\text{gvf}}(x,y,t)] \tag{23}$$

where Δt is the time step for each iteration. Equation (23) is simplified from (14) in [16] by ignoring the second term and can be rewritten as

$$\mathbf{f}_{\text{gvf}}(x,y,t+\Delta t) = \mathbf{f}_{\text{gvf}}(x,y,t) + \Delta t \mu \times [\nabla^2 u_{\text{gvf}}(x,y,t), \nabla^2 v_{\text{gvf}}(x,y,t)]. \tag{24}$$

The steady-state solution is achieved iteratively from the initialization $\mathbf{f}_{\text{gvf}}(x,y,0) = \nabla f(x,y)$. On a discrete grid, the Laplacian operator can be approximated by

$$\begin{aligned} \nabla^2 u_{\text{gvf}}(x,y,t) &= u_{\text{gvf}}(x+1,y,t) \\ &\quad + u_{\text{gvf}}(x-1,y,t) + u_{\text{gvf}}(x,y+1,t) \\ &\quad + u_{\text{gvf}}(x,y-1,t) - 4u_{\text{gvf}}(x,y,t) \\ \nabla^2 v_{\text{gvf}}(x,y,t) &= v_{\text{gvf}}(x+1,y,t) \\ &\quad + v_{\text{gvf}}(x-1,y,t) + v_{\text{gvf}}(x,y+1,t) \\ &\quad + v_{\text{gvf}}(x,y-1,t) - 4v_{\text{gvf}}(x,y,t). \end{aligned} \tag{25}$$

Substituting (25) into (24) gives an iterative solution in the form of the following convolution:

$$\begin{aligned} \mathbf{f}_{\text{gvf}}(x,y,t+1) &= \begin{bmatrix} 0 & \mu & 0 \\ \mu & 1-4\mu & \mu \\ 0 & \mu & 0 \end{bmatrix} * \mathbf{f}_{\text{gvf}}(x,y,t) \\ &= \Lambda_\mu * \mathbf{f}_{\text{gvf}}(x,y,t). \end{aligned} \tag{26}$$

where we assume $\Delta t = 1$ without loss generality. According to the GVF stability restriction, μ must be not larger than $1/4$ by making $\Delta x = \Delta y = 1$. We can expand (26) further, obtaining

$$\mathbf{f}_{\text{gvf}}(x,y,t) = \underbrace{\Lambda_\mu * \cdots * \Lambda_\mu}_{t} * \mathbf{f}_{\text{gvf}}(x,y,0) = \Lambda_\mu^t * \nabla f(x,y) \tag{27}$$

where t is integer, Λ_μ^t denotes the sequential convolution of t Λ_μ. The gradient of edge map f can be approximated by

$$\begin{aligned} \nabla f(x,y) &= \mathbf{k}_\nabla * f(x,y) \\ &= \frac{1}{2}[f(x+1,y) - f(x-1,y) \\ &\quad f(x,y+1) - f(x,y-1)] \end{aligned} \tag{28}$$

where

$$\mathbf{k}_\nabla = \frac{1}{2}\begin{bmatrix} & [0,1] & \\ [1,0] & [0,0] & [-1,0] \\ & [0,-1] & \end{bmatrix}. \tag{29}$$

Using a different discrete gradient approximation, such as the Sobel operator, will result a slightly different $\mathbf{k}_\nabla$. Therefore, (27) can be rewritten as

$$\mathbf{f}_{\text{gvf}}(x,y,t) = (\Lambda_\mu^t * \mathbf{k}_\nabla) * f(x,y) = \mathbf{k}_\mu^t * f(x,y). \tag{30}$$

By comparing (30) with the corresponding VFC (14), we can see that the GVF field in homogeneous regions of the image is a special case of VFC with kernel $\mathbf{k}_\mu^t$. The standard external force, i.e., the gradient of edge map f, is also a special case of VFC,

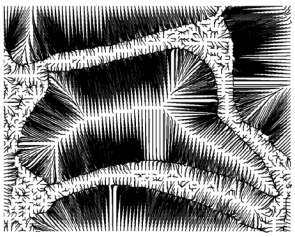

Fig. 4. Streamlines generated that mimic the GVF field for the edge map of Fig. 13 using mixed VFC filed with $\phi = \sqrt{\mu}$.

where the kernel is $\mathbf{k}_\nabla$. This connection provides a possible avenue to acceleration of the GVF calculation. Furthermore, we can mimic the GVF field using a mixed VFC field with $\phi = \sqrt{\mu}$, which is exemplified in Fig. 4. This example also demonstrated the fact that the kernel is crucial to the resulting VFC field. The essential difference between the GVF kernel $\mathbf{k}_\mu^t$ and the kernels employed with VFC is that the GVF kernel $\mathbf{k}_\mu^t$ has much smaller tails. A kernel with small tails tends to shrink the capture range of strong edges in the corresponding VFC field, since the influence of the FOI decreases as the tail decreases.

IV. Results and Analysis

We demonstrate several desirable properties of the VFC snakes in the results. The GVF snakes have gained tremendous popularity due to their ability to address a few difficulties appeared in previous snakes. Therefore, we also compare the VFC snakes results with the GVF snakes results. The magnitude function used in those experiments is $m_1(x, y)$ with $\gamma = 1.7$. We used $\alpha = 0.5, \beta = 0.1$ and $\tau = 0.5$ for all snakes in our experiments.

A. Capture Range and Convergence to Concavity

We use the U-shape example, which is also shown in [16], in our experiment. As shown in Fig. 5, both the VFC snake and the GVF snake are capable of capturing the boundary concavity from a far-off initialization, which demonstrates that both snakes have a large capture range and concavity convergence property. The two force fields are barely distinguishable from each other in this example; especially the vectors within the concavity in both force fields have a downward component to attract the snakes to the concavity, shown in the right column of Fig. 5.

In practical implementation, the capture range of the GVF field is influenced by two parameters: the smoothness parameter μ and the number of iterations. Although we know that the capture range increases as μ and the number of iterations increase, there is no specified relationship available to the user. If the user underestimates those parameters, the snakes may not converge correctly. Therefore, those parameters are usually overestimated in practice, which wastes computing time. In contrast, the capture range of the VFC field is determined by the capture range R of the vector field kernel.

B. Initialization Sensitivity

As we see in Fig. 5, both the VFC snake and the GVF snake can be initialized far away outside the object. Furthermore, in order to compare with the GVF snake initialization examples given in [16], Fig. 6 shows a set of initialization placed across and inside the boundary, with which the VFC snake converge correctly. These examples demonstrate that the VFC snake is insensitive to initialization and capable of converging into boundary concavities.

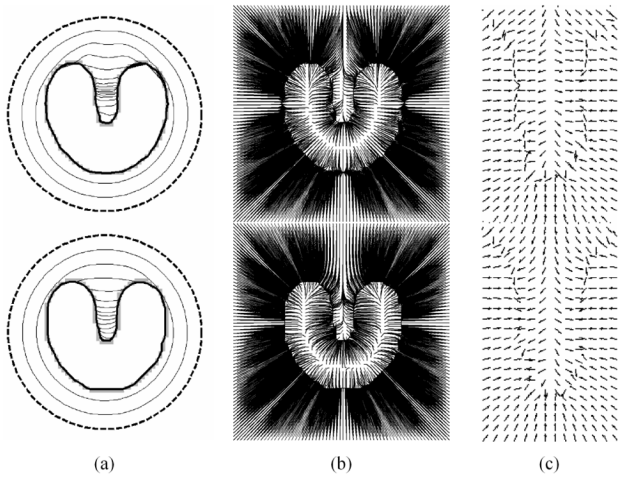

Fig. 5. Top (bottom) row, from left to right: (a) convergence of the GVF (VFC) snake, (b) streamlines generated from the GVF (VFC) field, and (c) magnified GVF (VFC) field within the concavity.

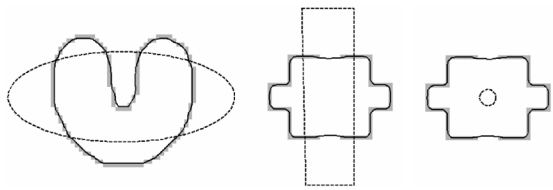

Fig. 6. (Dashed lines) Initial curves and (solid lines) the VFC snake results are superposed with the edge maps.

C. Computational Cost

If we represent the vectors as complex numbers, the VFC field can be calculated by convolving a complex matrix with the edge map, which can be accelerated by way of the FFT and the IFFT. Given an edge map of $N \times N$ pixels and a $(2R+1) \times (2R+1)$ vector field kernel, both of which are zero-padded to $(N+2R) \times (N+2R)$ to avoid wrap-around effects, the VFC field can be calculated in $O((N+2R)^2 \log(N+2R))$ multiples, which is determined by the complexity of 2-D FFT [31]. Typical values of R range from $N/8$ to $N/2$. The expense of VFC depends mainly on the size of the vector field kernel, whereas the computational cost of GVF depends by and large on the number of diffusion iterations. The GVF field needs $O(N^2)$ multiples within each iteration with a typical iteration number of N [16]. Therefore, in general, the complexity of the VFC field is $O(N^2 \log N)$, which compares favorably to the $O(N^3)$ complexity of the GVF computation. Fig. 7 compares the computational cost of VFC and GVF on different image size, from which we can see that GVF requires 3 to 10 times more computational expense than VFC. This experiment result was based on a Dell Dimension 9150 PC with Pentium D 2.8-GHz CPU, 1-GB RAM and MATLAB 7.

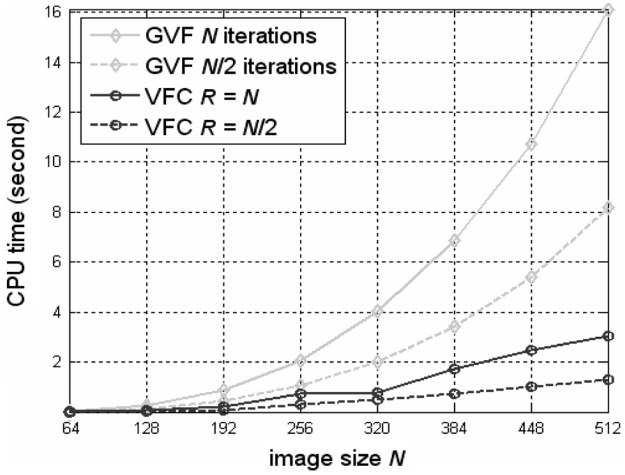

Fig. 7. Computational cost of GVF and VFC for an $N \times N$ image.

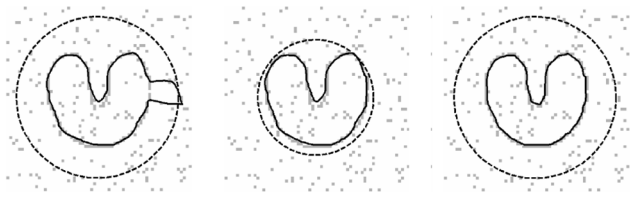

(a) (b) (c)

Fig. 8. (Solid lines) Impulse noise corrupted U-shape images overlapped with the results using (a), (b) the GVF snakes with (dashed lines) edge map $f(x,y) = -G_5(x,y) * I(x,y)$ from different initializations, where $G_\sigma(x,y)$ is a 2-D Gaussian function with standard deviation σ, and (c) the VFC snake with edge map $f(x,y) = -I(x,y)$. (a) $\mathrm{RMSE} = 3.20$; (b) $\mathrm{RMSE} = 0.43$; (c)$\mathrm{RMSE} = 0.24$.

D. Noise Sensitivity

To evaluate the noise sensitivity of GVF snakes and VFC snakes, we add impulse noise to the U-shape image in Fig. 5. Fig. 8 exhibits the noisy image superposed with initial snakes plotted in dashed lines. The GVF snake in Fig. 8(a) fails to converge to the U-shape because it is distracted by local impulse noise. Although a more proximal initialization provides an improved result in Fig. 8(b), the GVF snake does not capture some boundary features precisely, such as the concavity and the bottom right portion, which are distorted by the Gaussian filter. Alternatively, nonlinear filters may be applied to the edge map to eliminate noise, such as the feature weighted external energy [32].

Conversely, the VFC snake converges to the desired features without using a Gaussian (or similar) filter, as shown in Fig. 8(c). Although the noise outnumbers the edges in this example, the forces originated from the noise counteract each other and are overwhelmed by the forces generated from the true edges. Note that magnitude function $m_1(x,y)$ with $\gamma = 1.7$ is used in this example. If γ increases, the VFC snake may not converge because the influence of the edges is not strong enough to overcome the noise. As mentioned before, a smaller γ is desired for a higher noise level. To quantify the accuracy of the results, the root mean square error (RMSE) of the snake result is calculated. The error of a point on the snake is defined by the minimum distance between the point and U-shape in the noise-free image. As we see in Fig. 8, the VFC snake yields the smallest RMSE.

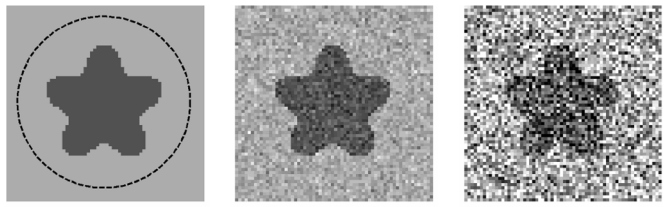

(a) (b) (c)

Fig. 9. (a) Noise-free image with (dashed line) the snake initialization. Example noise corrupted images with (b) 10- and (c) 0-dB SNR. (a) $\mathrm{SNR} = \infty$; (b) $\mathrm{SNR} = 10$ dB; (c) $\mathrm{SNR} = 0$ dB.

These results reveal the superior robustness to noise afforded by the VFC field.

Furthermore, we generate 50 images with same SNR for 11 different SNR levels (550 images in total) by adding zero mean Gaussian noise to a star-shaped grayscale image as shown in Fig. 9(a). Two examples with 10- and 0-dB SNR are shown in Fig. 9(b) and (c). GVF snakes and VFC snakes are deformed from the same initialization as shown in Fig. 9(a), and the RMSE is calculated after the snakes converge. The GVF snake result obtained from the noise-free image is taken as the ground truth. In our experiments, the edge map magnitude is normalized to $[0,1]$. After testing a range of μ values, we note that the GVF computation may be unstable for $\mu > 0.25$ and, therefore, use a maximal μ of 0.25. From Fig. 10, we can compare the performance of GVF snakes and VFC snakes using different filtering parameter values at different noise levels. By examining Fig. 10, we observe some salient features of the performance. First, the VFC snake with $\gamma = 2$ provides lowest overall RMSE, which is congruent with the claim that the VFC snakes are more robust to noise than GVF snakes. Second, using a larger standard deviation σ with the Gaussian filter does not necessarily improve the snake performance because the edge map may be over smoothed. For example, in Fig. 10(d), as the standard deviation of the Gaussian filter increases from 1 to 3, the associated RMSE values of the VFC snake with $\gamma = 2$ increase as well for SNRs larger than 1 dB. Third, reducing γ from 2.0 to 1.7 does not improve the performance of VFC snakes. The reason behind this lack of improvement is that a smaller γ encourages the snake to ignore noise as well as weak edges, which causes leakage problems similar to those encountered with pressure force snakes.

E. Application-Specific Implementation

The magnitude function can be modified to provide a tailored VFC field. We can include an anisotropic term in the magnitude function to obtain a VFC field similar to the *motion GVF* (MGVF) proposed in [7], which incorporates the motion direction inside the GVF energy to track cells. By initializing from the snake result in the previous frame, the MGVF field pushes the snake towards the motion direction in order to capture the shifted cell. The modified anisotropic magnitude function is given as

$$m_3(x,y) = c(x,y)m_i(x,y), \quad i = 1,2 \tag{31}$$

where $c(x,y)$ is the anisotropic term. In this experiment, $c(x,y)$ is defined as

$$c(x,y) = 1/[2 - \mathbf{d} \cdot \mathbf{n}(x,y)] \tag{32}$$

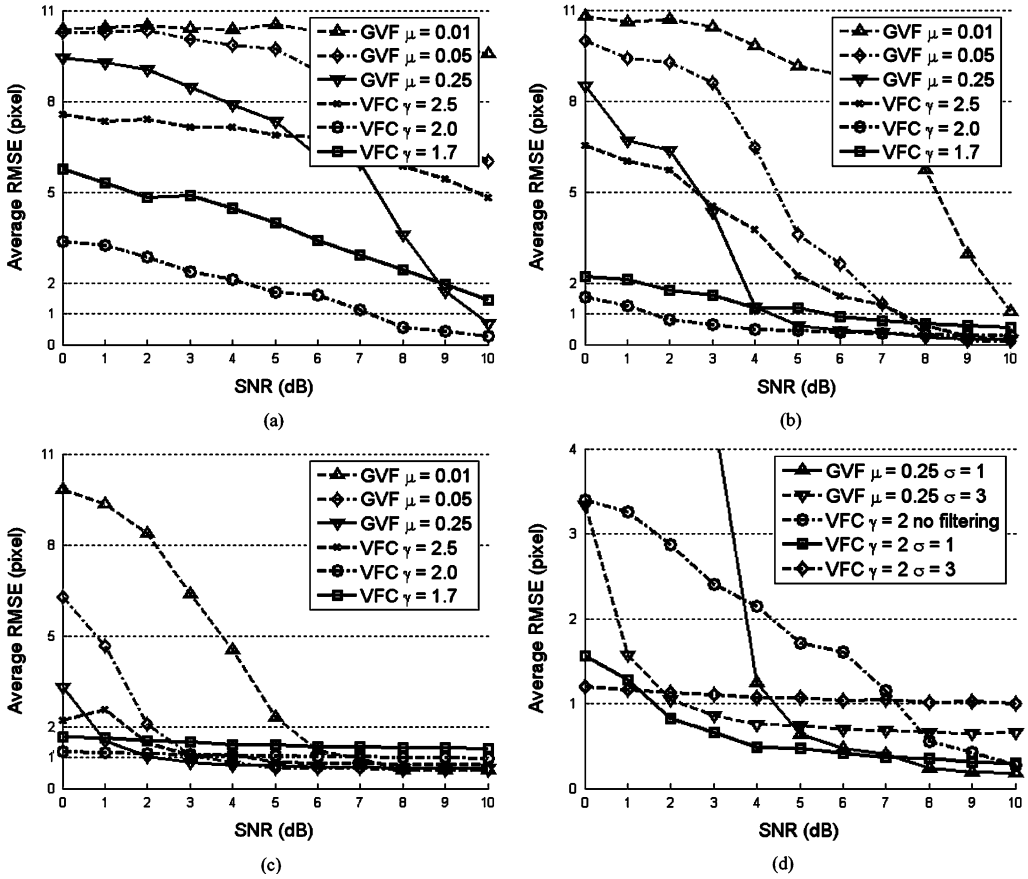

Fig. 10. Average RMSE of GVF and VFC with different parameters at different SNR levels using (a) nonfiltered edge map, and Gaussian filtered edge maps with (b) $\sigma = 1$ and (c) $\sigma = 3$. (d) Comparison of five selected snakes. The RMSE at each level is averaged over 50 synthetic images generated by randomly adding Gaussian noise to the noise-free image.

where $\mathbf{d}$ is a unit vector representing the motion direction, and $\cdot$ denotes the vector dot product. If $\mathbf{n}(x, y)$ and $\mathbf{d}$ have the same direction, $c(x, y)$ is close to 1; if they have the opposite direction, $c(x, y)$ is close to $1/3$. Therefore, like the MGVF field, the resulting VFC field is biased in the motion direction.

Fig. 11(a) shows a synthetic cell image with a displaced initialization, which represents the previous snake result. The GVF snake fails to capture the proper boundary and collapses into a point because of the isotropic gradient vector diffusion process, shown in Fig. 11(c). Whereas the VFC snake succeeds by using anisotropic magnitude function with motion direction $\mathbf{d} = [-1, 0]$, as shown in Fig. 11(b). The resulting anisotropic VFC force field is illustrated in Fig. 11(d), which is close to the MGVF force [7]. Note that the "origin point" where the streamlines emanate inside the ellipse in Fig. 11(b) is at the center, whereas the same point has been moved to the right in Fig. 11(d). This example demonstrates that VFC could be easily modified and improved for different applications.

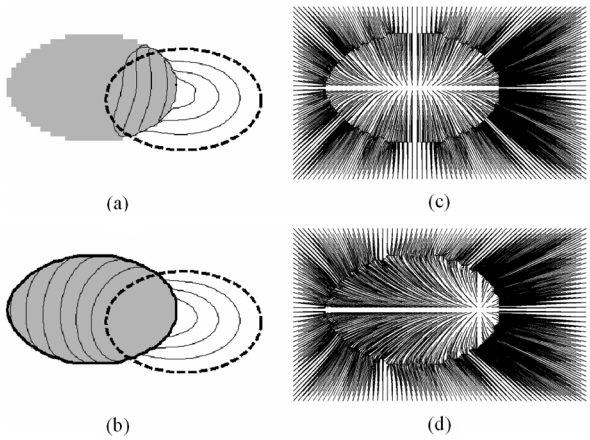

Fig. 11. Ellipse represents a synthetic cell with (dashed lines) initial snakes and (solid lines) results using (a) GVF and (b) VFC; streamlines generated from (c) the GVF field and (d) the VFC field.

F. VFC Active Surfaces

VFC can be easily extended to data of higher dimensionality. For n dimensions, the vector field kernel $\mathbf{k}(\mathbf{v}) : \mathbb{R}^n \rightarrow \mathbb{R}^n$ is defined as

$$\mathbf{k}(\mathbf{v}) = m(\mathbf{v}) \cdot \frac{-\mathbf{v}}{||\mathbf{v}||} \tag{33}$$

where $m(\mathbf{v}) : \mathbb{R}^n \rightarrow \mathbb{R}$ is the magnitude function, and $(-\mathbf{v})/(||\mathbf{v}||)$ is the unit vector pointing to the origin. The proposed magnitude functions (15)–(16) for 2-D can be rewritten as follows for n-D

$$m_1(\mathbf{v}) = (||\mathbf{v}|| + \varepsilon)^{-\gamma} \tag{34}$$

$$m_2(\mathbf{v}) = \exp(-||\mathbf{v}||^2/\zeta^2). \tag{35}$$

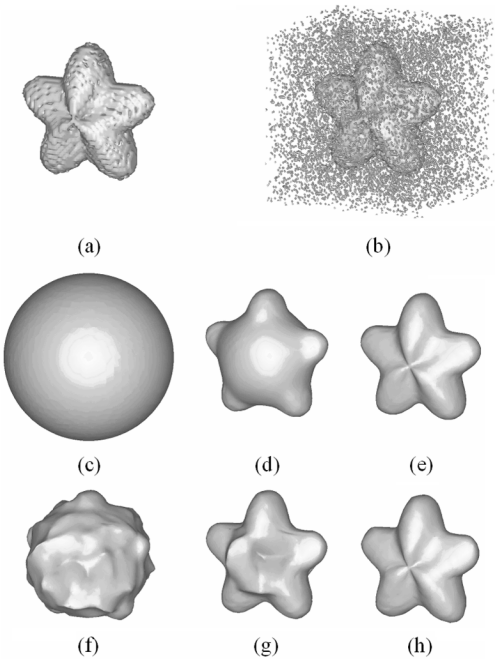

Fig. 12. Isosurface rendering of a 3-D star-like object in (a) a noise-free image and (b) an impulse noise corrupted image with -6 dB SNR. The deformation of the VFC active surface using (a) as edge map after (c) 0, (d) 20, and (e) 40 iterations. The deformation of the VFC active surface using (b) as edge map without filtering after (c) 0, (f) 20, (g) 40, and (h) 60 iterations.

Given the edge map $f(\mathbf{v}) : \mathbb{R}^n \rightarrow \mathbb{R}$ generated from the n-D image, the VFC field $\mathbf{f}_{\text{vfc}}(\mathbf{v}) : \mathbb{R}^n \rightarrow \mathbb{R}^n$ is given by calculating the convolution of each component of $\mathbf{k}(\mathbf{v})$ and the edge map

$$\begin{aligned}\mathbf{f}_{\text{vfc}}(\mathbf{v}) &= f(\mathbf{v}) * \mathbf{k}(\mathbf{v}) \\ &= [f(\mathbf{v}) * k_1(\mathbf{v}), \ldots, f(\mathbf{v}) * k_n(\mathbf{v})]. \end{aligned} \tag{36}$$

Examples of VFC active surfaces, a 3-D extension of VFC snakes, are illustrated in Fig. 12. We generated a 3-D star-like object in a 64^3 voxel image, which is shown in Fig. 12(a) using isosurface algorithm [33]. An active surface is initialized as a sphere far away outside the object, the deformation of which is shown in Fig. 12(c)–(e). The converged surface, as shown in Fig. 12(e), is smoother than the isosurface rendering as a result of the internal force influence in the active surface. Furthermore, impulse noise is randomly added to the image, which results -6 dB SNR, i.e., the noise is twice as much as the edges. The noise corrupted image, shown in Fig. 12(b) using isosurface algorithm, is used as the edge map for the VFC calculation without any filtering. With the same initialization, the VFC active surface overcomes the heavy noise and converges to the boundary correctly, as revealed in Fig. 12(c) and (f)–(h). By comparing Fig. 12(e) with Fig. 12(h), we can see that the upper left arm is slightly distorted because of the presence of the noise. The 3-D VFC field used in these examples is calculated using (34) with $\gamma = 3$. These examples demonstrate the feasibility of extending the VFC field to higher dimensions and the outstanding robustness to noise of VFC.

G. Real Images

We apply the VFC snakes to noisy magnetic resonance (MR) images of human ankles. External energies given by (2) and (3) can be used to calculate the edge map of the gray-level image. The Gaussian filter is employed to suppress the noise, whereas other techniques such as anisotropic diffusion [34], [35], morphological filtering, and the one proposed in [32] could also be applied to enhance the edge map. As shown in Fig. 14(a), the GVF snake becomes stuck in the interior and does not converge to boundary. The explanation can be found in Fig. 14(c)—the GVF snake tends to move in the vertical direction because there is little horizontal force component in the center area. In contrast, the VFC snake converges to the boundary concavities on the lower right precisely from the same initialization at the center, shown in Fig. 14(b). We also note that the GVF snake converges if the initialization is closer to the boundary. This anecdotal case exemplifies the robustness to initialization afforded by the VFC approach.

GVF snakes and VFC snakes are compared in an application of segmenting ultrasound images of a mouse heart (see Fig. 15). Furthermore, the dynamic directional GVF (DDGVF) snake [36], which employs a dynamic external force improved from the directional GVF [37], is used in this comparison. Speckle reducing anisotropic diffusion (SRAD) is employed to suppress the noise [35]. The VFC snake captures the endocardial border

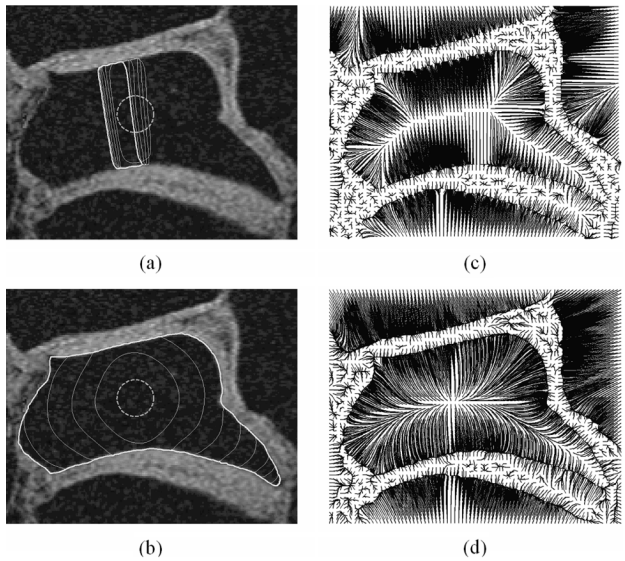

Fig. 13. MR image of a human ankle with (dashed lines) initial snakes and (solid lines) results using (a) GVF and (b) VFC; streamlines generated from (c) the GVF field and (d) the VFC field.

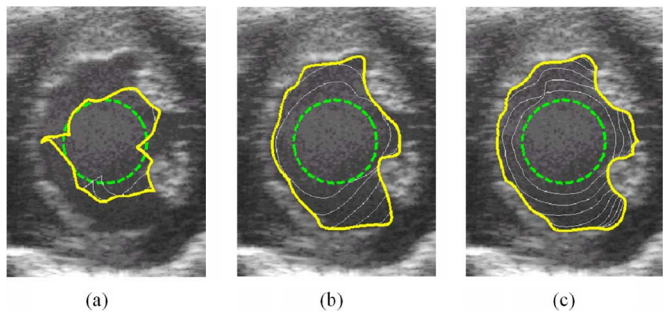

Fig. 14. Ultrasound image of a mouse heart with (dashed lines) initial snakes and (solid lines) results using (a) GVF, (b) DDGVF, and (c) VFC field. (a)$\text{RMSE} = 29.20$, (b) $\text{RMSE} = 5.26$, and (c) $\text{RMSE} = 2.68$.

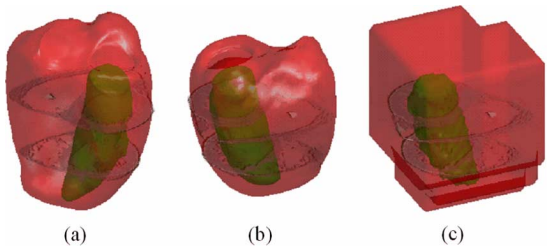

Fig. 15. (a), (b) Two views of VFC active surfaces segmentation result of the pericardium border (red) and endocardial border (green) deformed from (c) the initial surfaces. Two slices of the MR image of human heart is shown for reference.

accurately in 50 iterations, whereas the GVF snake is distracted by clutter and yields a significantly higher RMSE. Although the DDGVF snake improves the segmentation accuracy from the GVF snake with the cost of higher computational expense, the VFC snake has superior performance as demonstrated qualitatively in Fig. 15 and quantitatively by the lower RMSE. The RMSE is calculated by comparing to the manual segmentation by an expert.

We also demonstrate the segmentation result for a human heart 3-D MR image using VFC active surfaces in Fig. 13. The VFC active surfaces converge in 60 iterations and capture both borders accurately. A rotating 3-D movie showing the surfaces converging is available at http://viva.ee.virginia.edu/.

V. Conclusion

In this paper, a novel static external force for active contours, called the vector field convolution (VFC), has been introduced. The VFC field is calculated by convolving a vector field kernel with the edge map generated from the image. We proposed two classes of magnitude functions for the vector field kernel. We showed that the GVF field in homogeneous regions of the image is a special case of a VFC field. Several promising properties of VFC have been demonstrated by extensive examples. We have shown that the VFC snakes have large capture ranges, and converge to boundary concavities, similar to the GVF snakes. Additionally, the VFC snakes are less computationally expensive, more robust to noise and initialization than GVF snakes. VFC can also be easily customized and enhanced for different applications.

One possible drawback of VFC is that the weak edges might be overwhelmed by the strong edges along with the noise. We proposed the mixed VFC in this paper to alleviate this problem. Another solution is to scale the edge map that the weak edges have similar associated magnitude to that of the strong edges.

Acknowledgment

The authors would like to thank Dr. P. A. Helm and R. L. Winslow at the Center for Cardiovascular Bioinformatics and Modeling and Dr. E. McVeigh at the National Institutes of Health for the provision of the 3-D MR data.

References

[1] M. Kass, A. Witkin, and D. Terzopoulos, "Snakes-active contour models," *Int. J. Comput. Vis.*, vol. 1, pp. 321–331, 1987.

[2] D. Terzopoulos, A. Witkin, and M. Kass, "Constraints on deformable models-recovering 3D shape and nonrigid motion," *Artif. Intell.*, vol. 36, pp. 91–123, 1988.

[3] M. Gastaud, M. Barlaud, and G. Aubert, "Combining shape prior and statistical features for active contour segmentation," *IEEE Trans. Circuits Syst. Video Technol.*, vol. 14, no. 5, pp. 726–734, May 2004.

[4] J.-O. Lachaud and A. Montanvert, "Deformable meshes with automated topology changes for coarse-to-fine three-dimensional surface extraction," *Med. Image Anal.*, vol. 3, pp. 187–207, 1999.

[5] T. McInemey and D. Terzopoulos, "Topology adaptive deformable surfaces for medical image volume segmentation," *IEEE Trans. Med. Imag.*, vol. 18, no. 10, pp. 840–850, Oct. 1999.

[6] T. McInerney and D. Terzopoulos, "A dynamic finite element surface model for segmentation and tracking in multidimensional medical images with application to cardiac 4D image analysis," *Comput. Med. Imag. Graph.*, vol. 19, pp. 69–83, 1995.

[7] N. Ray and S. T. Acton, "Motion gradient vector flow: An external force for tracking rolling leukocytes with shape and size constrained active contours," *IEEE Trans. Med. Imag.*, vol. 23, no. 12, pp. 1466–1478, Dec. 2004.

[8] N. Ray, S. T. Acton, and K. Ley, "Tracking leukocytes in vivo with shape and size constrained active contours," *IEEE Trans. Med. Imag.*, vol. 21, no. 10, pp. 1222–1235, Oct. 2002.

[9] A. R. Mansouri, D. P. Mukherjee, and S. T. Acton, "Constraining active contour evolution via lie groups of transformation," *IEEE Trans. Image Process.*, vol. 13, no. 6, pp. 853–863, Jun. 2004.

[10] N. Paragios and R. Deriche, "Geodesic active contours and level sets for the detection and tracking of moving objects," *IEEE Trans. Pattern Anal. Mach. Intell.*, vol. 22, no. 3, pp. 266–280, Mar. 2000.

[11] T. F. Cootes, G. J. Edwards, and C. J. Taylor, "Active appearance models," *IEEE Trans. Pattern Anal. Mach. Intell.*, vol. 23, no. 6, pp. 681–685, Jun. 2001.

[12] T. F. Cootes, C. J. Talyor, D. H. Cooper, and J. Graham, "Active shape models—Their training and applications," *Comput. Vis. Image Understand.*, vol. 61, pp. 38–59, 1995.

[13] J. A. Sethian, *Level Set Methods and Fast Marching Methods: Evolving Interfaces in Computational Geometry, Fluid Mechanics, Computer Vision, and Materials Science*. Cambridge, U.K.: Cambridge Univ. Press, 1999.

[14] D. Terzopoulos and T. McInerey, "Deformable models in medical image analysis: A survey," *Med. Image Anal.*, vol. 1, pp. 91–108, 1996.

[15] J.-Y. Park, T. McInerney, D. Terzopoulos, and M.-H. Kim, "A non-self-intersecting adaptive deformable surface for complex boundary extraction from volumetric images," *Comput. Graph.*, vol. 25, pp. 421–440, 2001.

[16] C. Xu and J. L. Prince, "Snakes, shapes, and gradient vector flow," *IEEE Trans. Image Process.*, vol. 7, no. 3, pp. 359–369, Mar. 1998.

[17] C. Xu and J. L. Prince, "Generalized gradient vector flow external forces for active contours," *Signal Process.*, vol. 71, pp. 131–139, 1998.

[18] N. Paragios, O. Mellina-Gottardo, and V. Ramesh, "Gradient vector flow fast geometric active contours," *IEEE Trans. Pattern Anal. Mach. Intell.*, vol. 26, no. 3, pp. 402–407, Mar. 2004.

[19] B. Li and S. T. Acton, "Vector field convolution for image segmentation using snakes," presented at the IEEE Int. Conf. Image Processing, Atlanta, GA, 2007.

[20] L. D. Cohen and I. Cohen, "Finite-element methods for active contour models and balloons for 2-D and 3-D images," *IEEE Trans. Pattern Anal. Mach. Intell.*, vol. 15, no. 11, pp. 1131–1147, Nov. 1993.

[21] W. Press, S. Teukolsky, W. Vetterling, and B. Flannery, *Numerical Recipes in C*, 2nd ed. Cambridge, MA: Cambridge Univ. Press, 1992.

[22] A. Benson and D. J. Evans, "A normalized algorithm for solution of positive definite symmetric quindiagonal systems of linear equations," *ACM Trans. Math. Softw.*, vol. 3, pp. 96–103, 1977.

[23] T. McInerney and D. Terzopoulos, "Topology adaptive deformable surfaces for medical image volume segmentation," *IEEE Trans. Med. Imag.*, vol. 18, no. 10, pp. 840–850, Oct. 1999.

[24] A. Chakraborty, L. H. Staib, and J. S. Duncan, "Deformable boundary finding in medical images by integrating gradient and region information," *IEEE Trans. Med. Imag.*, vol. 15, no. 6, pp. 859–870, Dec. 1996.

[25] C. Xu, D. L. Pham, M. E. Rettmann, D. N. Yu, and J. L. Prince, "Reconstruction of the human cerebral cortex from magnetic resonance images," *IEEE Trans. Med. Imag.*, vol. 18, no. 6, pp. 467–480, Jun. 1999.

[26] J. Canny, "A computational approach to edge detection," *IEEE Trans. Pattern Anal. Mach. Intell.*, vol. PAMI-8, no. 6, pp. 679–714, Nov. 1986.
[27] D. Yuan and S. Lu, "Simulated static electric field (SSEF) snake for deformable models," presented at the Int. Conf. Pattern Recognition, Quebec, QC, Canada, 2002.
[28] J. W. Cooley and J. W. Tukey, "An algorithm for the machine calculation of complex Fourier series," *Math. Comput.*, vol. 19, pp. 297–301, 1965.
[29] H. Sorensen, D. Jones, M. Heideman, and C. Burrus, "Real-valued fast Fourier transform algorithms," *IEEE Trans. Acoust., Speech, Signal Process.*, vol. 35, no. 6, pp. 849–863, Jun. 1987.
[30] N. Otsu, "A threshold selection method from gray-level histograms," *IEEE Trans. Syst., Man, Cybern.*, vol. SMC-9, no. 1, pp. 62–66, Jan. 1979.
[31] P. Duhamel and M. Vetterli, "Fast Fourier transforms: A tutorial review and a state of the art," *Signal Process.*, vol. 19, pp. 259–299, 1990.
[32] B. Li and S. T. Acton, "Feature weighted active contours for image segmentation," presented at the Southwest Symp. Image Analysis and Interpretation, Denver, CO, 2007.
[33] W. E. Lorensen and H. E. Cline, "Marching cubes: A high resolution 3D surface construction algorithm," *Comput. Graph.*, vol. 21, pp. 163–169, 1987.
[34] S. T. Acton, "Multigrid anisotropic diffusion," *IEEE Trans. Image Process.*, vol. 7, no. 3, pp. 280–291, Mar. 1998.
[35] Y. Yu and S. T. Acton, "Speckle reducing anisotropic diffusion," *IEEE Trans. Image Process.*, vol. 11, no. 11, pp. 1260–1270, Nov. 2002.
[36] J. Cheng and S. W. Foo, "Dynamic directional gradient vector flow for snakes," *IEEE Trans. Image Process.*, vol. 15, no. 6, pp. 1563–1571, Jun. 2006.
[37] J. Tang, S. Millington, S. T. Acton, J. Crandall, and S. Hurwitz, "Surface extraction and thickness measurement of the articular cartilage from MR images using directional gradient vector flow snakes," *IEEE Trans. Biomed. Eng.*, vol. 53, no. 5, p. 896, May 2006.

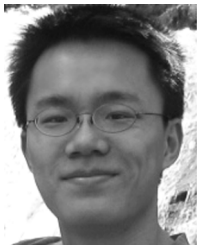

Bing Li (S'06) received the B.S. degree in electrical and computer engineering from Peking (Beijing) University, Beijing, China, in 2003, and the M.S. and Ph.D. degrees in electrical engineering from the University of Virginia, Charlottesville, in 2005 and 2007, respectively.

He is working in the RAPID division for KLA-Tencor Corporation. His research interests include medical image analysis, image segmentation, active models, and target tracking.

Scott T. Acton (SM'99) graduated from Oakton High School, Vienna, Virginia, in 1984. He received the B.S. degree in electrical engineering from Virginia Tech, Blacksburg, in 1988, as a Virginia Scholar, and the M.S. and Ph.D. degrees in electrical and computer engineering from the University of Texas at Austin in 1990 and 1993, respectively, where he was a student of Prof. A. Bovik.

He has worked in industry for AT&T, Oakton, VA; the MITRE Corporation, McLean, VA; Motorola, Inc., Phoenix, AZ; and in academia for Oklahoma State University, Stillwater. Currently, he is Professor of electrical and computer engineering and biomedical engineering at the University of Virginia (UVA), Charlottesville. His research interests include anisotropic diffusion, basketball, active contours, biomedical segmentation problems, and biomedical tracking problems.

Dr. Acton is an active participant in the IEEE, currently serving as Associate Editor for the IEEE TRANSACTIONS ON IMAGE PROCESSING and, formerly, as Associate Editor for the IEEE SIGNAL PROCESSING LETTERS. He was the 2004 Technical Program Chair and the 2006 General Chair for the Asilomar Conference on Signals, Systems and Computers. At UVA, he was named the Outstanding New Teacher in 2002, Faculty Fellow in 2003, and Walter N. Munster Chair for Intelligence Enhancement in 2003.